

Supplementary Information for

A diamond voltage imaging microscope

D. J. McCloskey^{1*†}, N. Dontschuk^{1†}, A. Stacey^{1,2}, C. Pattinson¹, A. Nadarajah¹, L. T. Hall¹, L. C. L. Hollenberg^{1,3}, S. Praver¹, D. A. Simpson^{1*}.

¹School of Physics, University of Melbourne; Parkville, VIC 3010, Australia.

²School of Science, RMIT University; Melbourne, VIC 3001, Australia.

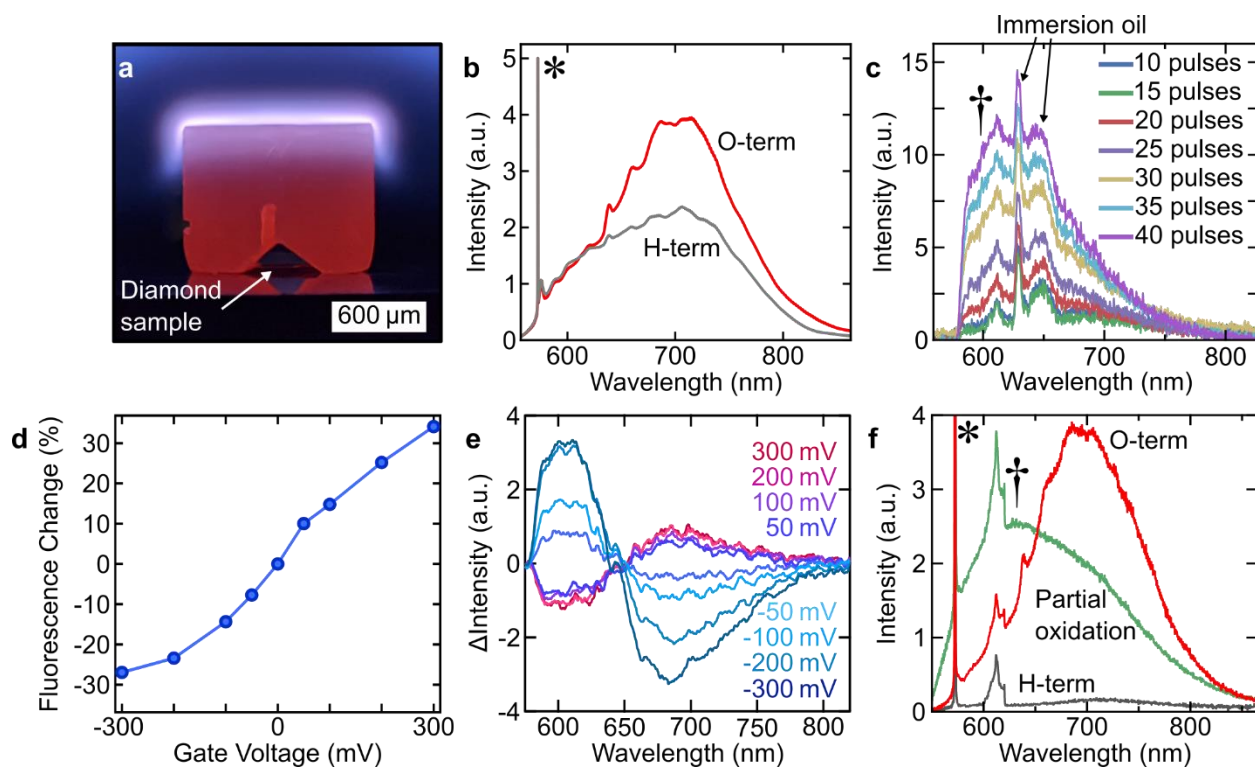
³Centre for Quantum Computation and Communication Technology, School of Physics, University of Melbourne, Parkville, VIC 3010, Australia

† These authors contributed equally to this work.

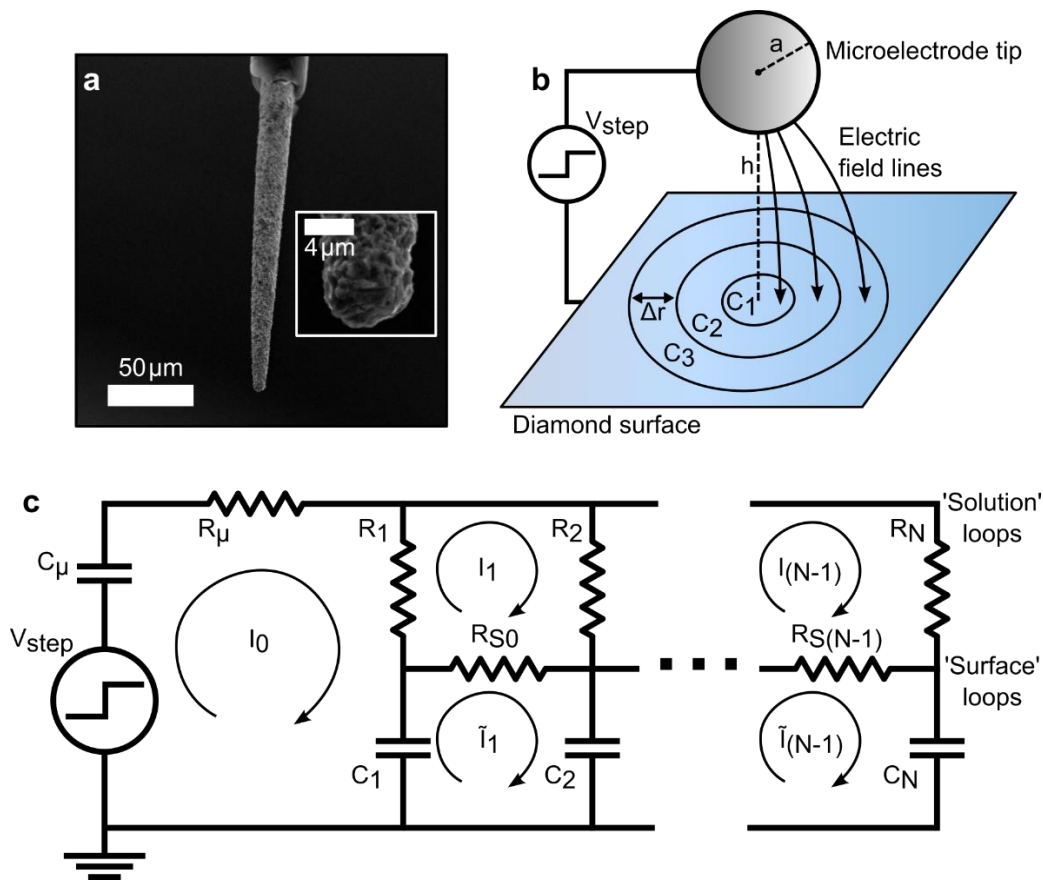
*Corresponding authors. Email: dan.mccloskey@unimelb.edu.au, simd@unimelb.edu.au

Table of Contents

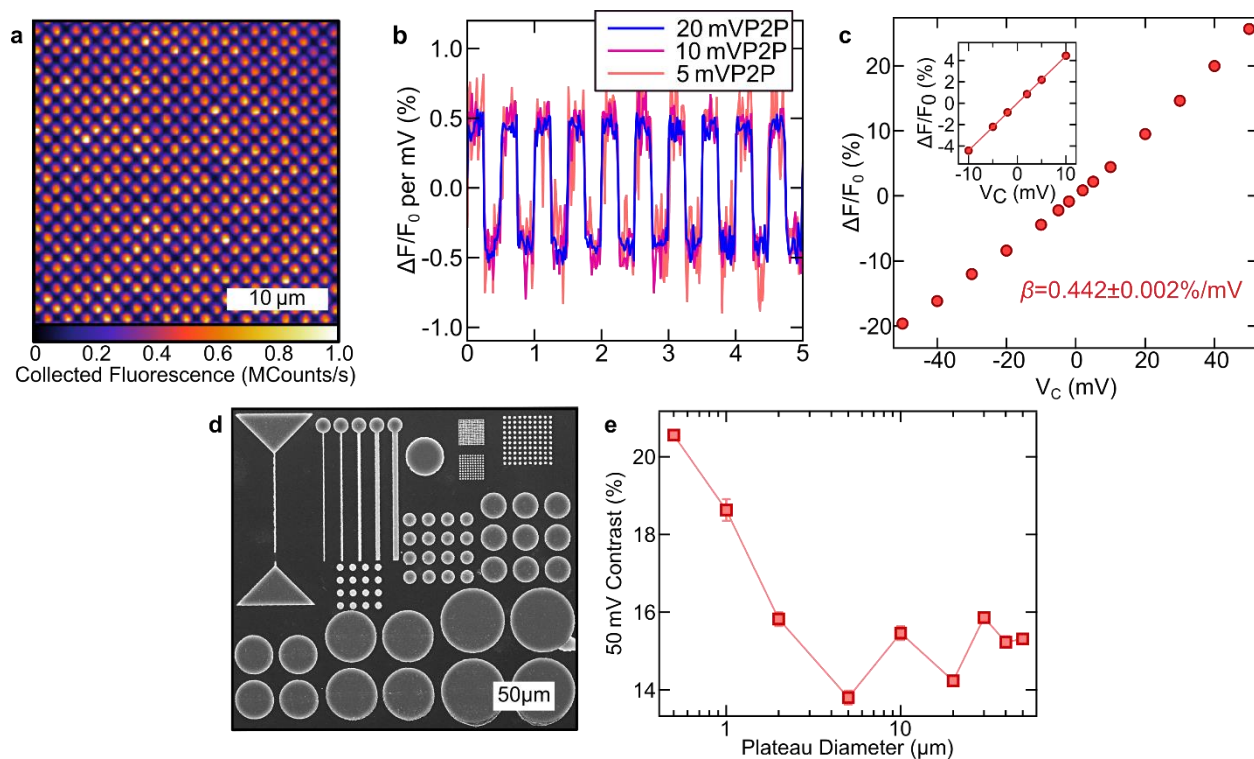
Supplementary Figure 1. Sample hydrogenation and additional spectroscopic characterization	3
Supplementary Figure 2. Platinum/iridium microelectrode and equivalent RC circuit model of microelectrode charge injection imaging using a DVIM	4
Supplementary Figure 3. Additional characterization of optrode-patterned DVIM surface	5
Supplementary Figure 4. Long-term stability of the diamond voltage imaging microscope	6
Supplementary Figure 5. Reciprocal sensitivity of a single optimized diamond optrode	7
Supplementary Figure 6. Additional fast signal detection data	8
Supplementary Figure 7. Effect of poly-D-lysine (PDL) coating on DVIM responsivity and voltage sensitivity	9
Supplementary Table 1. Parameters used in the equivalent RC circuit simulation of microelectrode charge injection imaging using the DVIM.	10
Supplementary Table 2. Voltage sensitivities, spatial resolutions, and sensitivity thresholds for biological signal detection used to produce Figure 4 in the main text.	11
Supplementary Table 3. Parameters used in the calculation of the sensitivity limit of a single diamond optrode	12
Supplementary Methods. Equivalent circuit model of microelectrode charge injection	13
Supplementary Note 1. Derivation of shot noise limited sensitivity equation.....	18
Supplementary Note 2. Estimating existing technological sensitivities and signal thresholds	19
Supplementary Note 3. Limit of voltage sensitivity from a single diamond optrode	20
Supplementary Note 4. Compatibility with biological adhesion promoters	23
Supplementary Video 1. DVIM recording of spatiotemporal voltage transient.....	24
Supplementary References	24



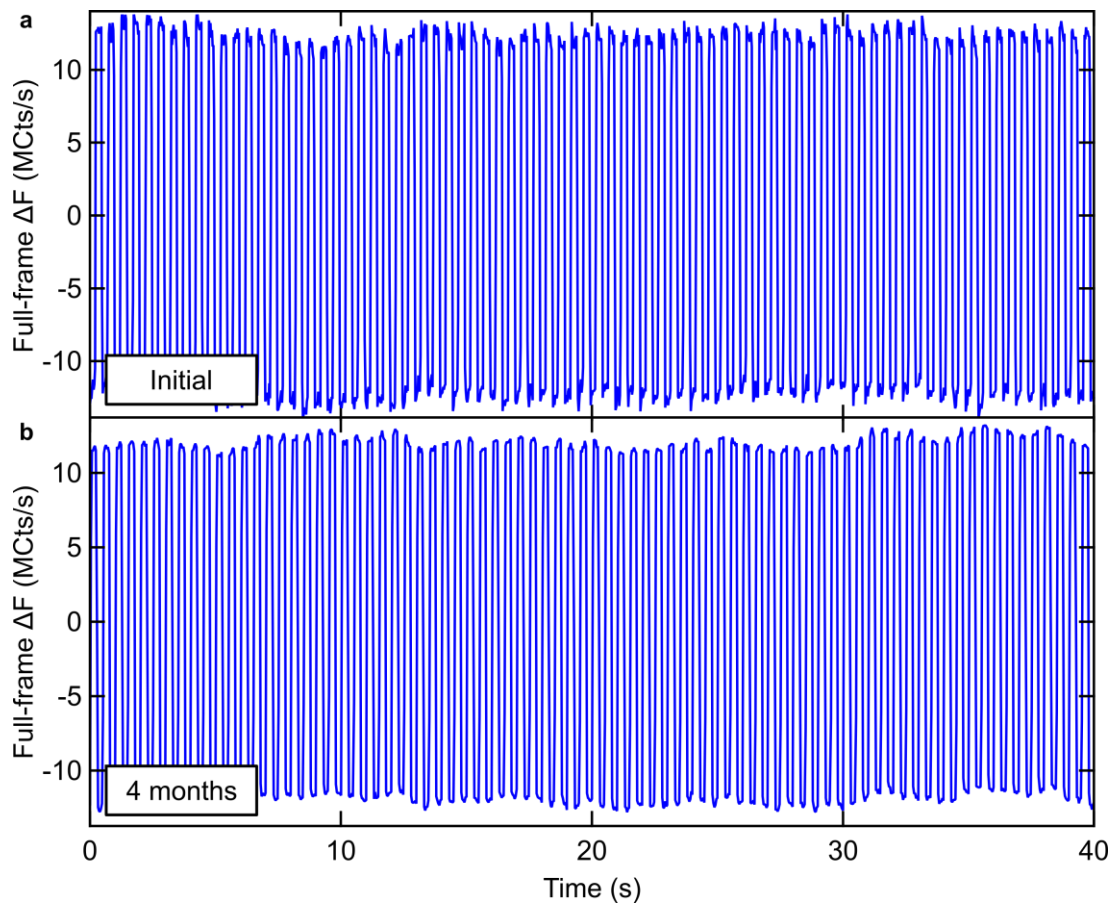
Supplementary Figure 1: Sample hydrogenation and additional spectroscopic characterization. (a) Photograph of a diamond sample undergoing hydrogen-termination by indirect hydrogen plasma exposure in a microwave plasma-enhanced chemical vapor deposition reactor using a perforated molybdenum shield to prevent plasma from contacting the diamond surface. (b) Fluorescence spectra before and after indirect plasma hydrogen-termination of an electronic-grade diamond sample containing a shallow NV ensemble created by 4 keV, $10^{13}/\text{cm}^2$ ion implantation and annealing at 950°C for 4 hours. Oxygen-termination was performed by acid boiling (Methods). Spectra are normalized to the first-order Raman emission line indicated by the asterisk (*). (c) Progressive increase in baseline (0V solution-gate potential) NV fluorescence upon application of successive electrochemical oxidation pulses. Features at 625 nm and 650 nm are fluorescence from immersion oil, while the 2nd order diamond Raman emission is indicated by the dagger (†). (d) Relative change in NV fluorescence as a function of solution gate voltage obtained by integrating the raw spectra used to produce Figure 1h in the main text. (e) Fluorescence spectral changes upon application of solution gate voltages in PBS for an $\approx 10^{11}/\text{cm}^2$ NV ensemble created by 2 keV, $1e^{13}/\text{cm}^2$ nitrogen ion implantation which has been oxidized beyond its maximal sensitivity point (≈ 70 oxidation pulses), showing interconversion between NV^- and NV^0 . (f) Raw fluorescence spectra of the primary sample studied in the main text before hydrogenation (O-term, red curve), after hydrogenation (H-term, gray), and after surface oxidation to the optimal voltage sensing region (partial oxidation, green curve). First-order Raman emission (*) and second-order Raman emission (†) features are shown. Spectra are normalized to the first-order Raman lines.



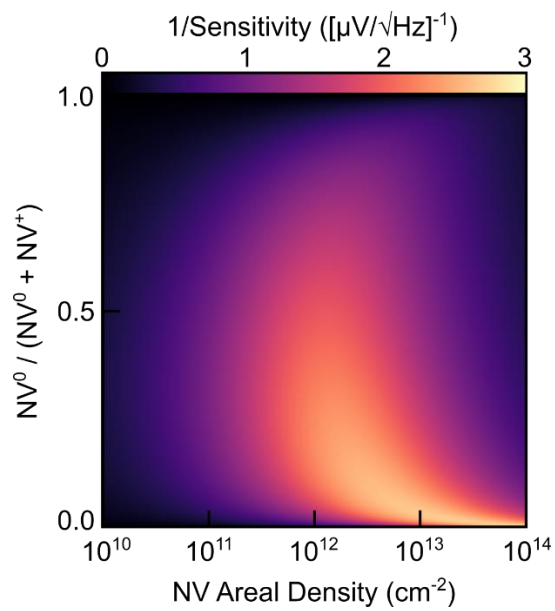
Supplementary Figure 2: Platinum/iridium microelectrode and equivalent RC circuit model of microelectrode charge injection imaging using a DVIM. (a) Scanning electron micrograph of the platinum/iridium microelectrode used in the experiments. Inset: A higher magnification image of the electrode tip. (b) Schematic illustration of the model used to replicate the microelectrode imaging experiments. The microelectrode is approximated as an ideal spherical voltage source, and the diamond surface is discretized into annular elements of width Δr , each having its own capacitance. (c) Equivalent circuit model of the microelectrode imaging experiments, with counterclockwise loop currents used in the solution of the circuit illustrated. Symbols are described in the Supplementary text.



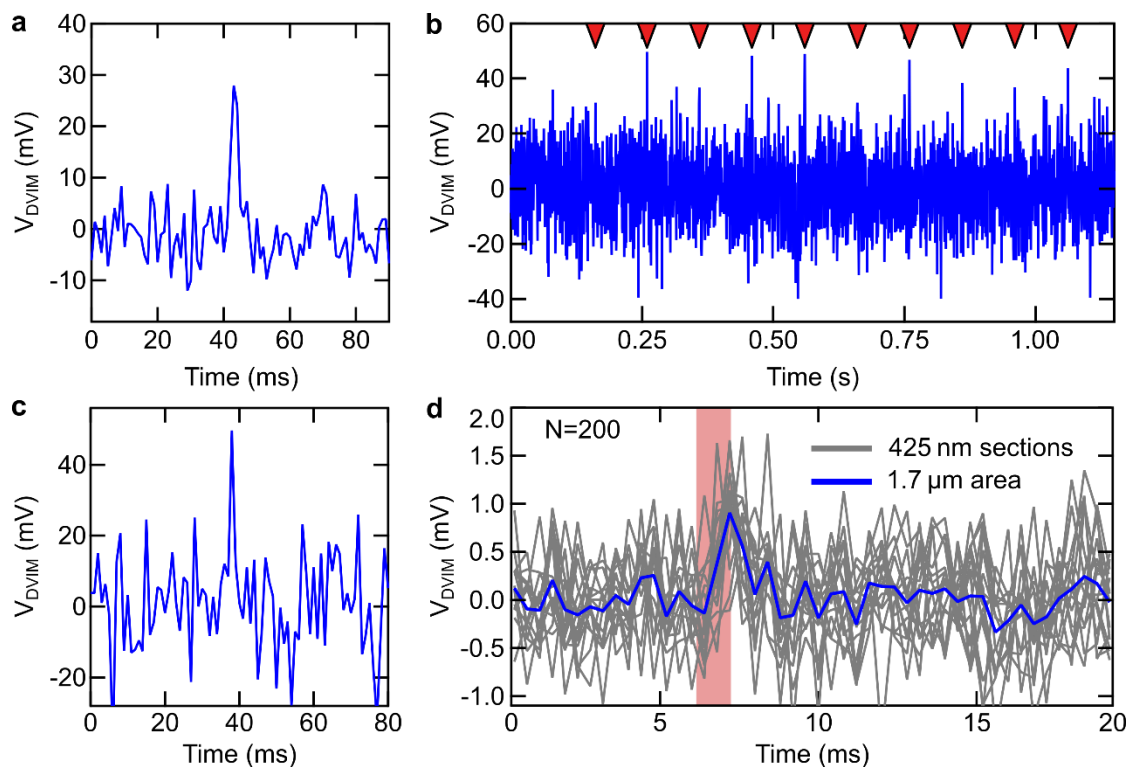
Supplementary Figure 3: Additional characterization of optrode-patterned DVIM surface. (a) Scanning confocal microscopic image of a section of an optrode array, showing uniform fluorescence emission intensity from each optrode. (b) Fluorescence time-traces for a single diamond optrode subject to a varying square-wave solution gate voltage, normalized to the 0V fluorescence and the amplitude of the applied signal. (c) Fluorescence contrast vs. solution gate voltage integrated over the whole field-of-view shown in Figures 3b and 3d of the main text. Inset: Zoom-in about gate voltages from -10 mV to 10 mV, straight line shows a linear fit to the data, from which a responsivity (slope) of $0.442 \pm 0.002\%/mV$ was extracted. (d) Scanning-electron micrograph of the circular test structures used to probe the relationship between fluorescence contrast and optrode diameter. Ribbon and bow-tie structures in the top left were not used in this work. (e) 50 mV fluorescence contrast as a function of diameter for the circular plateaus shown in (d). Where not visible, error bars are smaller than the data points.



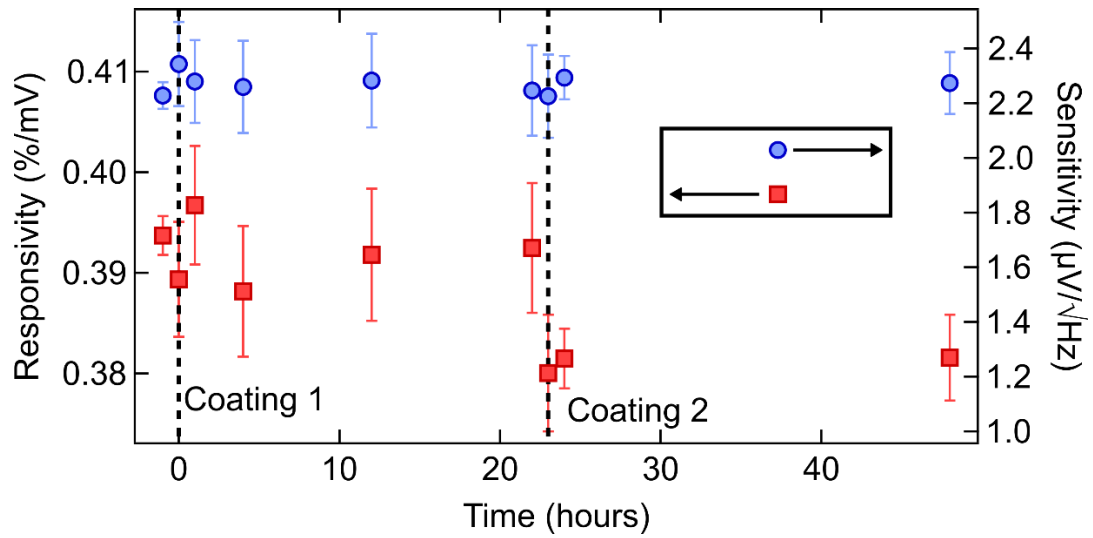
Supplementary Figure 4: Long-term stability of the diamond voltage imaging microscope. Full-frame integrated fluorescence (40× oil-immersion objective lens, 128×128 pixel field-of-view corresponding to roughly 13.74 μm×13.74 μm) from the diamond optrode array shown in Figure 3 of the main text. A 20 mV peak-to-peak square wave at 2 Hz was applied to the sample in PBS using a platinum electrode at the onset of measurements (a) and after 4 months of sample characterization (b). Slow (2-5 seconds) intensity fluctuations are due to fluctuations in laser excitation power. The apparent reduction in noise from (a) to (b) is the result of a longer camera frame exposure time for panel (b) (40 ms) compared to panel (a) (30 ms).



Supplementary Figure 5: Reciprocal sensitivity of a single optimized diamond optrode. The modeled optrode utilizes the fluorescence interconversion between NV^0 and the non-fluorescent NV^+ charge states, and is plotted as a function of the equilibrium (no applied voltage) population of the NV^0 state and the areal density of the NV ensemble. For the equation used to produce this image and the additional parameters employed, see Supplementary Note 3 and Supplementary Table 3 respectively.



Supplementary Figure 6: Additional fast signal detection data. (a) Zoom of a single 1ms pulse recorded over the 4x4 optrode array. (b) Voltage signals at the diamond surface recorded by the single optrode in closest proximity to the platinum/iridium microelectrode in response to a 10Hz train of 1 ms square pulses with an amplitude of 400 mV. Red triangles denote the pulse rising edges (the pulse train was manually triggered at around 0.15 s). (c) Zoom of a single pulse from the single-optrode trace shown in (b). (d) Sub-millivolt signal recording, identical to Figure 4c in the main text but shown here for $N=200$ integrations. The shaded region indicates the applied 5 mV square pulse 'on' time. All traces are presented without filtering.



Supplementary Figure 7: Effect of poly-D-lysine (PDL) coating on DVIM responsivity and voltage sensitivity. Measurements were performed using integrated fluorescence over a flat, 55 μm square area of the DVIM surface. Vertical dashed lines indicate applications of PDL coatings as described in Supplementary Note 4. Responsivity, sensitivity, and their uncertainties were measured/calculated according to our standard protocol (Methods).

Parameter	Name	Value (Units)	Measured/Calculated/ /Chosen
κ_S	Bulk solution resistivity	42 ± 2 (k Ω ·cm)	Calculated
κ_D	Specific surface resistivity	21 ± 2 (M Ω)	Calculated
C_D	Diamond areal capacitance	2.3 ± 0.6 (μ F/cm ²)	Calculated
C_μ	Microelectrode capacitance	14.5 (nF)	Measured
a	Microelectrode radius	4 (μ m)	Measured
h	Microelectrode standoff	2 (μ m)	Calculated/Chosen
R_μ	Microelectrode resistance	2.5 (Ω)	Calculated
V_{step}	Applied voltage step	100 (mV)	Chosen
Δr	Radial space step	1 (μ m)	Chosen
N	Number of radial steps	1500	Chosen
Δt	Time step	1 (ms)	Chosen
β_{FOV}	Average fluorescence contrast responsivity	0.25 (%/mV)	Measured
$\sqrt{2}\sigma_L$	Laser spot 1/e decay length	77.8 (μ m)	Measured

Supplementary Table 1: Parameters used in the equivalent RC circuit simulation of microelectrode charge injection imaging using the DVIM.

Technology (Threshold)	1kHz Sensitivity ($\mu\text{V}/\sqrt{\text{Hz}}$)	Resolution (μm)	Reference
Passive MEA	0.02	1410	1
CMOS MEA	0.05	18.0	2
CMOS MEA	0.03	20.0	3
CMOS MEA	0.1	16.0	4
CMOS MEA	0.25	15.0	5
CMOS MEA	0.1	28.0	6
(Intracellular AP)	894	-	7
(Extracellular AP)	5	-	8

Supplementary Table 2: Voltage sensitivities, spatial resolutions, and sensitivity thresholds for biological signal detection used to produce Figure 4 in the main text. Estimated sensitivities/resolutions of voltage-sensitive indicators are based on their optical diffraction-limited resolution combined with the lack of published demonstrations of extracellular action potential detection at that resolution at the time of writing.

Parameter	Name	Value (Units)	Reference
e	Electron charge	1.602×10^{-19} (C)	-
k	Boltzmann constant	8.617×10^{-5} (eV/K)	-
T	Temperature	300 (K)	-
C_{EDL}	Hydrogen-terminated diamond electrolytic double-layer capacitance	2 ($\mu\text{F}/\text{cm}^2$)	⁹
R	Photon count-rate for a single NV^0 center	1.275 (MHz)	^{10,11}
A_{op}	Fluorescent surface area of a single diamond optrode	4.783×10^{-8} (cm^2)	-
ρ	Nitrogen implant density	10^{14} (cm^{-2})	-

Supplementary Table 3: Parameters used in the calculation of the sensitivity limit of a single diamond optrode.

Supplementary Methods 1: Equivalent circuit model of microelectrode charge injection

The macro-and-mesoscopic dynamics of electrodiffusion and boundary layer formation in dilute electrolyte solutions are of a fundamentally nonlinear nature and can be described by the Poisson-Nernst-Planck system of equations¹². For small signals, these dynamics can also be approximated by linear equivalent circuit models^{13,14}, which is the approach followed here. Such models are commonly employed in the description of electrode-electrolyte interfaces on multi-electrode arrays^{7,15-17}, though we stress that linear circuit models in general cannot replicate the complete electrochemical dynamics of diffuse systems, especially over long time periods¹². This is evident in Figure 2d in the main text. Nonetheless, an equivalent circuit provides a useful means of conceptualizing the function of the DVIM as an optical measurement of the charge/voltage across a capacitor. More importantly, it allows us to verify the veracity of DVIM measurements to first order by confirming that any deleterious back-action by the sensor, which could for instance be caused by photovoltaic effects¹⁸, provides only higher-order perturbations to the expected RC dynamics. We model the injection of charge into dilute saline solution by discretizing the diamond surface into N annular elements which are axially aligned with the microelectrode tip, shown in Supplementary Figure 2a, modelled here as an ideal spherical voltage source of radius a as sketched in Supplementary Figure 2b.

The potentials applied in these experiments lie within the roughly ± 0.5 V water window of hydrogenated diamond gated by a platinum electrode¹⁹, meaning no Faradaic current flows through either electrode. We therefore model the diamond surface and microelectrode as ideal capacitors. The dilute solution is approximated as a purely resistive bulk element with resistivity κ_S . To derive an expression for the approximate resistance which connects the microelectrode to each annular surface element, we assume that hole carriers in the grounded diamond surface rearrange to screen the electric field produced by the microelectrode tip on a much shorter timescale than the rearrangement of solvated charges in the solution. Under this assumption, the electric field produced by this configuration at the instant the external voltage is applied will be given (via the method of images) by the field of an ideal dipole with separation $2d = 2(a + h)$ where h is the height of the surface of the sphere (i.e., the tip of the microelectrode) from the diamond and a is the radius of the sphere. The electric field $\mathbf{E}(r)$ at the diamond surface will therefore be oriented perpendicular to the surface, with a magnitude that depends on the radial distance r from the axis of cylindrical symmetry given by:

$$\mathbf{E}(r) = \frac{-2dq\hat{z}}{4\pi\epsilon(d^2 + r^2)^{3/2}}$$

Where q is the total charge carried by the sphere, ϵ is the dielectric permittivity of the solution, and \hat{z} is a unit vector oriented perpendicular to the diamond surface. At the instant the voltage is applied (before capacitive elements in the model have acquired any charge), current flow is simply given by the generalized Ohm's law:

$$\mathbf{J} = \frac{\mathbf{E}}{\kappa_S}$$

Where \mathbf{J} is the current density. The total current flowing into the i^{th} annular surface element, I_i , is then equal to the integral of the current density over that element:

$$I_i = \int_0^{2\pi} \int_{r_i}^{r_i+\Delta r} (\mathbf{J} \cdot \hat{\mathbf{z}}) r dr d\theta = \frac{2\pi}{\kappa_S} \frac{2dq}{4\pi\epsilon} \int_{r_i}^{r_i+\Delta r} \frac{r}{(d^2 + r^2)^{3/2}} dr$$

$$= \frac{dq}{\kappa_S \epsilon} \left(\frac{1}{\sqrt{d^2 + r_i^2}} - \frac{1}{\sqrt{d^2 + (r_i + \Delta r)^2}} \right)$$

Where r_i is the inner radius of the i^{th} annular element and Δr is the step size of the discrete radial domain. To obtain an approximate expression for q , note that the potential profile for a dipole comprised of two point charges located at the centers of the real and virtual spherical electrodes is:

$$V_{dipole}(r, z) = \frac{q}{4\pi\epsilon} \left(\frac{1}{\sqrt{r^2 + (z - d)^2}} - \frac{1}{\sqrt{r^2 + (z + d)^2}} \right)$$

At a distance a from the point charge, we specify that the potential will be equal to the applied voltage V_{step} . For simplicity, we consider $r = 0$ for this analysis:

$$V_{dipole}(0, d - a) = V_{step} = \frac{q}{4\pi\epsilon} \left(\frac{1}{\sqrt{a^2}} - \frac{1}{\sqrt{(2d - a)^2}} \right)$$

This gives an expression for q in terms of V_{step} , which can be substituted into the expression for I_i to yield:

$$I_i = \left[\frac{2\pi da(2d - a)}{\kappa_S(d - a)} \left(\frac{1}{\sqrt{d^2 + r_i^2}} - \frac{1}{\sqrt{d^2 + (r_i + \Delta r)^2}} \right) \right] V_{step}$$

Invoking Ohm's law for a linear resistive element, we may finally interpret the term in square brackets above to be the reciprocal of the effective resistance R_i between the microelectrode and the i^{th} surface segment:

$$R_i = \left[\frac{2\pi da(2d - a)}{\kappa_S(d - a)} \left(\frac{1}{\sqrt{d^2 + r_i^2}} - \frac{1}{\sqrt{d^2 + (r_i + \Delta r)^2}} \right) \right]^{-1}$$

The electrodiffusion of charge tangential to the diamond surface is approximated in our model by adding a resistor between the capacitances of adjacent diamond surface elements. We introduce a specific effective surface resistivity κ_D as a parameter which encapsulates the coupled charge transport dynamics of the solvated ions in the electrolytic double-layer at the diamond surface and the two-dimensional hole gas confined to the first few nanometers below the surface. The surface resistance R_{Si} between the i^{th} and $i+1^{\text{th}}$ surface segments is then given by:

$$R_{Si} = \frac{\kappa_D \Delta r}{2\pi r_{i+1}}$$

such that the resistance is proportional to the chosen radial length element and inversely proportional to the circumference through which charge transport occurs. The areal capacitance of the diamond surface C_D , given by the series capacitance of the electrolytic double-layer and the bulk quantum capacitance (the capacitance associated with the energy-dependent filling of electronic states²⁰), is also treated as a parameter. In general, the interfacial capacitance of the hydrogenated diamond/electrolyte interface varies as a function of both pH and voltage⁹. In this experiment, the pH of the dilute buffered saline

solution is fixed at approximately 7, so this dependence is ignored in the model. The voltage dependence of C_D has been measured to be small when potentials lower than -200 mV are applied using an Ag/AgCl reference electrode²¹. To find out what this means for our apparatus, wherein the diamond is held at zero bias with respect to a large platinum metal counter electrode in its normal sensing configuration, we measured the potential of an Ag/AgCl reference electrode (eDAQ) with respect to the diamond (while the diamond was connected externally to the platinum electrode) in dilute buffered saline and obtained a value of -360 ± 10 mV. This value doubles as a measurement of the difference in electrochemical half-cell potentials between platinum metal and the Ag/AgCl electrode and agrees with previously reported values²². We therefore assume in this model that C_D is constant within the range of experimentally accessed voltage perturbations (± 100 mV). C_D is used to obtain the capacitance of each annular surface element C_i via:

$$C_i = \pi C_D (r_{i+1}^2 - r_i^2)$$

We solve for the time dynamics of the equivalent circuit, shown in Supplementary Figure 2c, using the standard techniques of mesh analysis. Kirchoff's law requires that the potential drops around each closed loop of the circuit sum to zero, resulting in the following linear system:

$$\begin{aligned} -I_0(R_\mu + R_1) + I_1 R_1 &= \frac{Q_\mu}{C_\mu} + \frac{Q_1}{C_1} - V_{step} \\ I_0 R_1 - I_1(R_1 + R_2 + R_{S1}) + \tilde{I}_1 R_{S1} + I_2 R_2 &= 0 \\ I_1 R_{S1} - \tilde{I}_1 R_{S1} &= \frac{Q_2}{C_2} - \frac{Q_1}{C_1} \\ I_1 R_2 - I_2(R_2 + R_3 + R_{S2}) + \tilde{I}_2 R_{S2} + I_3 R_3 &= 0 \\ \vdots & \\ I_{N-2} R_{N-1} - I_{N-1}(R_{N-1} + R_N + R_{S(N-1)}) + \tilde{I}_{N-1} R_{S(N-1)} &= 0 \\ I_{N-1} R_{S(N-1)} - \tilde{I}_{N-1} R_{S(N-1)} &= \frac{Q_N}{C_N} - \frac{Q_{N-1}}{C_{N-1}} \end{aligned}$$

Where I_i and \tilde{I}_i are the circulating currents in the i^{th} solution and surface loops respectively (see Supplementary Figure 2c), Q_i is the stored charge on the i^{th} surface segment, V_{step} is the applied voltage step amplitude, and values subscripted with “ μ ” denote those of the microelectrode. Defining

$$\mathbf{I} = (I_0, I_1, \tilde{I}_1, I_2, \tilde{I}_2, \dots, I_{N-1}, \tilde{I}_{N-1}),$$

$$\mathbf{Q} = (Q_\mu, Q_1, Q_2, \dots, Q_{N-1}, Q_N), \text{ and}$$

$$\mathbf{V} = (V_{step}, 0, 0, \dots)$$

where \mathbf{V} is $2N - 1$ elements long, we can rewrite this system as:

$$\hat{\mathbf{A}}\mathbf{I} = \hat{\mathbf{B}}\mathbf{Q} - \mathbf{V}$$

Where the linear operators \hat{A} and \hat{B} are defined to yield the system above. The charges on each capacitor in the circuit evolve in time according to the first-order differential equations:

$$\begin{aligned}\dot{Q}_\mu &= I_0 \\ \dot{Q}_1 &= I_0 - \tilde{I}_1 \\ \dot{Q}_2 &= \tilde{I}_1 - \tilde{I}_2 \\ &\vdots \\ \dot{Q}_{N-1} &= \tilde{I}_{N-2} - \tilde{I}_{N-1} \\ \dot{Q}_N &= \tilde{I}_{N-1}\end{aligned}$$

Where we may again write this as:

$$\dot{\mathbf{Q}} = \hat{\mathbf{C}}\mathbf{I}$$

With a corresponding linear operator $\hat{\mathbf{C}}$. We approximately solve this system by time-stepping using a first-order implicit Euler method. This gives us:

$$\mathbf{Q}_{i+1} - \dot{\mathbf{Q}}_{i+1}\Delta t = \mathbf{Q}_{i+1} - \hat{\mathbf{C}}\mathbf{I}_{i+1}\Delta t = \mathbf{Q}_{i+1} - \hat{\mathbf{C}}\hat{\mathbf{A}}^{-1}(\hat{\mathbf{B}}\mathbf{Q}_{i+1} - \mathbf{V})\Delta t = \mathbf{Q}_i$$

Where the subscript i denotes the value at the i^{th} time step, with the step size given by Δt . Moving the term containing the applied potential \mathbf{V} to the right-hand side, we obtain:

$$(\hat{\mathbf{I}} - \Delta t\hat{\mathbf{C}}\hat{\mathbf{A}}^{-1}\hat{\mathbf{B}})\mathbf{Q}_{i+1} = \mathbf{Q}_i - \Delta t\hat{\mathbf{C}}\hat{\mathbf{A}}^{-1}\mathbf{V} = \hat{\mathbf{D}}\mathbf{Q}_{i+1}$$

Where $\hat{\mathbf{I}}$ is the identity and $\hat{\mathbf{D}} = \hat{\mathbf{I}} - \Delta t\hat{\mathbf{C}}\hat{\mathbf{A}}^{-1}\hat{\mathbf{B}}$. Finally, the implicit Euler step is given by:

$$\mathbf{Q}_{i+1} = \hat{\mathbf{D}}^{-1}(\mathbf{Q}_i - \Delta t\hat{\mathbf{C}}\hat{\mathbf{A}}^{-1}\mathbf{V})$$

Once the charges are calculated at the i^{th} time step, the potentials measured by the DVIM at each annular segment are determined by dividing the charges by their corresponding diamond surface capacitances.

We use a capacitance of 14.5 nF for the Pt/Ir microelectrode based on impedance specifications provided by the manufacturer. We vary the solution resistivity, surface resistivity, and diamond areal capacitance in our model to obtain agreement between the calculated time dynamics and the experimentally measured voltages at the diamond surface. The optimization is performed using a brute-force minimization to obtain an initial guess for the parameter values. The guess is then used as an input to the nonlinear least-squares minimization function (running the Levenberg-Marquardt minimization algorithm) available in the `scipy.optimize` library. A selection of 5 radially-averaged experimental voltage curves (measured radially from the microelectrode tip location) taken at different times following the application of the voltage step were used to compute the residuals for the simulated curves (Figure 2f). To better reflect our experimental conditions which used a camera exposure time of 6 ms and 24×24 pixel binning, the simulated curves at each point in time are averaged over the preceding 6 ms and averaged in space over 5.68 μm . We chose a value of 1 μm for Δr and 1500 for N so the total surface area of the simulated diamond would approximately match the surface area of the measured sample. Uncertainties in the fit parameters were obtained by fitting to the sum and difference of the experimental data with the experimental uncertainty, then taking the mean difference between the resulting values and those

obtained from the primary data. We note that systematic errors in the model, for instance those resulting from the approximation of the microelectrode as spherical, are likely to be more significant than statistical errors. A value of $h = 2 \mu\text{m}$ resulted in good agreement between the simulated curves and the experiment, while larger values of h yielded considerably less localization of the voltage transient than was measured by the DVIM. The values of all parameters used/obtained for the final simulation are given in Supplementary Table 1.

To model the full-frame fluorescence response of the device, shown in Figure 2d of the main text, we consider only the first K annular elements in our simulation domain with a radius smaller than half our camera's field of view (FOV) of $\approx 184 \mu\text{m}$. We use the measured aggregate contrast responsivity of the flat DVIM surface of $0.25 \%/mV$ for the contrast responsivity across the whole FOV, denoted by β_{FOV} . The relative change in fluorescence intensity over the FOV, $\Delta F_{FOV}/F_{FOV}$ is then calculated via:

$$\frac{\Delta F_{FOV}(t)}{F_{FOV}} = \frac{\beta_{FOV}}{T_{FOV}} \sum_{i=0}^K \pi V_i(t) (r_{i+1}^2 - r_i^2) e^{-\frac{(r_i + \Delta r)^2}{2\sigma_L^2}}$$

Where $V_i(t)$ is the voltage at the i^{th} annular diamond surface element at time t , while the exponential term and factor σ_L account for the Gaussian profile of our widefield laser illumination. A value of $\sigma_L = 55 \mu\text{m}$ was estimated by fitting a Gaussian function to an image of the average diamond fluorescence. The factor T_{FOV} is the normalized baseline (zero voltage) fluorescence, given by:

$$T_{FOV} = \sum_{i=0}^K \pi (r_{i+1}^2 - r_i^2) e^{-\frac{(r_i + \Delta r)^2}{2\sigma_L^2}}$$

Supplementary Note 1: Derivation of shot noise limited sensitivity equation

As with other optical voltage imaging techniques²³, the signal of interest produced by our sensor is the relative change in measured fluorescence, $\Delta F/F_0$, where F_0 is the baseline fluorescence. For a linearly responsive sensor, as is the case here for small voltages (see Figure 2b of the main text), ΔF can be expressed as the product of the baseline fluorescence, the voltage signal ΔV , and a constant of proportionality which we term here the responsivity β :

$$\frac{\Delta F}{F_0} = \frac{\beta F_0 \Delta V}{F_0} = \beta \Delta V$$

Under the assumption of a shot noise limited optical measurement, the noise of the sensor is sampling-frequency independent with a standard-deviation equal to \sqrt{N} where N is the mean number of photons collected in a single measurement period. In our measurements, this average is the baseline fluorescence F_0 , resulting in a relative noise level of $1/\sqrt{F_0}$. For a change in voltage to be detectable, the optical signal-to-noise ratio must exceed unity:

$$\beta \Delta V \sqrt{F_0} > 1$$

The smallest detectable voltage ΔV_{min} is found by taking the limit as the SNR approaches one, thus:

$$\Delta V_{min} = \frac{1}{\beta \sqrt{F_0}}$$

The baseline fluorescence can be expressed as the product of the sampling time Δt and the baseline fluorescence count rate I_0 . Rearranging, we obtain the expression for the shot noise limited sensitivity η , which has the expected units of $V/\sqrt{\text{Hz}}$:

$$\eta = \Delta V_{min} \Delta t = \frac{1}{\beta \sqrt{I_0}}$$

Supplementary Note 2: Estimating existing technological sensitivities and signal thresholds

To obtain reasonable ranges for the resolutions and sensitivities of existing passive and CMOS multi-electrode array systems, we use reported values sourced from the contemporary literature. To estimate sensitivity thresholds for intracellular and extracellular action potential detection, we used published time traces of intra/extracellular action potentials measured using multi-electrode arrays, taking one half of the waveform duration to be the measurement period and one half of the peak-to-peak amplitude of the waveform to be the signal amplitude. Our obtained values, as well as the appropriate references, are included in Supplementary Table 2. Our estimated sensitivity/resolution range for voltage-sensitive indicators was based on their optical diffraction-limited resolution combined with a lack of published demonstrations of extracellular action potential detection using this technology at the time of writing.

Supplementary Note 3: Limit of voltage sensitivity from a single diamond optrode

We recall from Equation 1 that the shot noise limited sensitivity η of our DVIM is given in general by (see Supplementary Note 1):

$$\eta = \frac{1}{\beta \sqrt{I_0}}$$

Where β is the responsivity and I_0 is the fluorescence count rate. For a single optrode, this can be expanded as:

$$I_0 = \rho \chi A_{op} DR$$

Where ρ is the density of implanted nitrogen, A_{op} is the fluorescent surface area of the optrode, χ is the nitrogen-to-NV conversion ratio, D is the fractional population of the charge state of interest, and R is the fluorescence count rate from a single defect in this charge state. In equilibrium, the position of the Fermi level with respect to the adiabatic charge state transition energies of the NV determines D , but due to band-bending not all NVs in a thick ensemble will be affected by changes in the diamond surface potential. In the ideal limiting scenario, NV centers would be situated in a delta-doped profile at the diamond surface, thereby maximizing the total number of defects which undergo charge state conversion upon a change in the surface potential. Equivalently, we could also consider the case of a flat band-profile near the surface and a non-delta-doped layer, which would have the same effect. With the assumption that all NV defects lie at the same charge-state transition energy in the bandgap (i.e., their density is low enough that sub-band formation effects can be considered negligible), the equilibrium fractional charge-state population of the ensemble is given by the Fermi-Dirac distribution:

$$D = f_D(V_S) = \frac{1}{1 + \exp\left(\frac{E_D + E_F - eV_S}{kT}\right)}$$

Where e is the electron charge, E_D is the adiabatic charge-state transition energy of the defect, E_F is the Fermi level, V_S is the diamond surface potential, k is the Boltzmann constant, and T is the ambient temperature. The change in the charge-state population with respect to a change in surface potential is therefore:

$$\frac{dD}{dV_S} = \frac{df_D(V_S)}{dV_S} = \frac{\frac{e}{kT} \exp\left(\frac{E_D + E_F - eV_S}{kT}\right)}{\left(1 + \exp\left(\frac{E_D + E_F - eV_S}{kT}\right)\right)^2} = \frac{e}{kT} D(1 - D)$$

Employing the definition of the responsivity gives:

$$\beta = \frac{1}{D} \frac{dD}{dV_G} = \frac{1}{D} \frac{dD}{dV_S} \frac{dV_S}{dV_G}$$

where V_G is the solution gate voltage. We can express the change in surface potential with respect to the gate voltage as the potential drop across an effective capacitance which characterizes the (surface) voltage dependence of the number of occupied electronic states within the bulk material. This capacitance, commonly denoted ‘quantum capacitance’ in the literature²⁰, appears in series with the electrolytic double-layer capacitance of the diamond surface, C_{EDL} , so the change in the diamond surface potential (in equilibrium) can be found using the expression for the potential drop across one element of a two-capacitor voltage divider:

$$\frac{dV_s}{dV_G} = \frac{C_{EDL}}{C_{EDL} + C_Q}$$

Where C_Q is the diamond quantum capacitance. In general, any change to the diamond surface charge will induce a compensatory (opposite) change in the bulk charge, where some of this charge will be sourced from changes to the hole density and some will result from charge state conversion of NVs or other defects. In the limit where all compensatory charge comes from holes, no change in fluorescence will occur and the DVIM has no voltage sensitivity. We concern ourselves here with the opposite limit, the ‘best case scenario’ wherein any change to the diamond surface charge will cause an identical change to the charge state population of the defect of interest. This scenario could be approached in practice through careful engineering of the depth distribution and areal density of the NV ensemble. The limiting case allows us to calculate the quantum capacitance in terms of D and the areal density of NVs:

$$C_Q = \frac{dD}{dV_s} \rho \chi e = \frac{\rho \chi e^2}{kT} D(1 - D)$$

Substituting the above expressions into that for the responsivity yields:

$$\beta = \frac{eC_{EDL}(1 - D)}{kTC_{EDL} + \rho \chi e^2 D(1 - D)}$$

Finally, the shot noise limited sensitivity for an ideal diamond optrode will be given by:

$$\eta_{ideal} = \frac{kTC_{EDL} + \rho \chi e^2 D(1 - D)}{eC_{EDL}(1 - D) \sqrt{\rho \chi A_{op} DR}}$$

Saturation count-rates for single NV centers embedded in tapered diamond nanopillars have been measured at 1.7 MCts/s¹⁰. Using the fact that NV⁰ is about 3/4 as bright as NV⁻ due to a longer fluorescence lifetime¹¹, we can assume that a maximal fluorescence count-rate from each NV center in our optrodes R of 1.275 MCts/s can be achieved under ideal circumstances, for instance through the use of a more efficient excitation wavelength for NV⁰, microlenses, or antireflective (e.g., gradient refractive index) patterning on the backside of the diamond chip²⁴⁻²⁶. One obvious inefficiency of the optrodes described in this work is that they do not contain NV ensembles in their sidewalls, however it has previously been

shown that collection efficiencies from sidewall-embedded ensembles are also enhanced compared to flat diamond surfaces²⁷. By increasing the use of available chip real-estate by utilizing the optrode sidewalls as well as their tips to host NV ensembles, we estimate that the number of NVs in each (in other words the optrode area A_{op}) can be increased by more than 12 times given an optrode diameter of 700 nm and a depth of 2 μm . Substituting a realistic⁹ value for C_{EDL} of 2 μFcm^{-2} , we can obtain η_{ideal} as a function of the equilibrium NV^0 charge-state population fraction D and the NV areal density given by $\rho\chi$. These are sensible parameters to vary, as this work has demonstrated that control over D is possible through surface oxidation techniques (Figure 1 of the main text) while it is known that $\text{N}\rightarrow\text{NV}$ conversion ratios can be increased using electron irradiation^{28,29} or appropriate co-doping³⁰. Our chosen parameters are collated in Supplementary Table 3. Plotting the resulting values of η_{ideal} in Supplementary Figure 5, the best physically allowable single-optrode sensitivity for an areal NV density of $10^{13}/\text{cm}^2$ (corresponding to 100% conversion of a $10^{13}/\text{cm}^2$ nitrogen implantation) is 375 $\text{nV}/\sqrt{\text{Hz}}$, about 145 times more sensitive than the best device produced here and well below the approximately 5 $\mu\text{V}/\sqrt{\text{Hz}}$ required for single-shot recording of extra-cellular action potentials from cultured mammalian neurons⁸. We include values of the NV areal density up to $10^{14}/\text{cm}^2$ in the plot to show that only marginal improvements in sensitivity will result from increasing the NV density beyond $10^{13}/\text{cm}^2$.

Supplementary Note 4: Compatibility with biological adhesion promoters

The practical use of diamond, both hydrogen and oxygen-terminated, as a substrate material for electrical recordings of cultured cells typically relies on the use of coatings which promote the adhesion of the cells in question to the diamond surface^{31–35}. These coatings can take the form of proteins which attach to the membrane proteins of the cells or of cationic polymers which promote direct electrostatic attachment to the cell membrane^{31–35}. Due to their ability to modify the surface charge of a substrate, cationic polymers have been observed to be capable of modifying the near-surface band-bending and NV charge state in oxygen-terminated fluorescent nanodiamonds³⁶. The band-bending effects of such molecules on the sensor reported here, which employs hydrogen-terminated bulk single-crystal diamond, have yet to be explored. Here we have investigated one such cationic polymer, poly-D-lysine (PDL), which is commonly used to promote the adhesion of cultured neurons to a variety of substrates^{37,38}, including diamond³³. We used PDL with a molecular weight distribution of 50,000 Da to 150,000 Da (Gibco) which was diluted to 50 µg/mL in DI water. The DVIM chip was coated with PDL in accordance with the specifications provided by the manufacturer. Briefly, we applied 2 mL of coating solution to the PDMS fluid well (diameter of 1 cm) containing the diamond sample. The sample was incubated at room temperature for 1 hour before being rinsed 3 times with DI water. The mean voltage responsivity and calculated shot noise limited sensitivity of a 55 µm×55 µm flat area of the DVIM surface were measured using our standard protocol (Methods) prior to coating, immediately post-coating, and then intermittently over the next 48-hour period.

As shown in Supplementary Figure 7, we observed no loss of either responsivity or sensitivity within our experimental uncertainty over this period. After 24 hours, we applied a second coating of PDL using the same protocol as the first, at which point we observed an approximately 2.5% reduction in the device responsivity. This loss of contrast persisted over the next 24-hour period, but all throughout the experiment our calculated sensitivity remained unchanged within uncertainty. This is due to a commensurate increase in the baseline NV fluorescence with the reduction of fluorescence contrast, which suggests the net effect of the PDL coating is a reduction in the areal density of negative charge at the diamond surface (equivalent to the application of a small DC bias to the uncoated device) leading to a reduction of the near-surface band-bending and an increase in the baseline NV⁰ population. This interpretation is consistent with the compensation of negative surface adsorbates on the diamond by the positive ligands of the PDL coating, but the minimal nature of the effect would suggest that the effective areal charge density provided by the PDL is not sufficiently large to compete with the density of the native adsorbate layer. We also note that only a single coating of PDL is typically employed in cell culturing experiments. From this preliminary data we conclude that DVIM technology is compatible with PDL coatings, but the observed effect, as well as the potential for using near-surface NV charge-state measurements to probe interactions between hydrogenated diamond and other adhesion promoting molecules, merits further investigation.

Supplementary Video 1: DVIM recording of spatiotemporal voltage transient. The voltage measured by the DVIM due to the application of a 100mV step to a Pt/Ir microelectrode positioned 2 μm from the diamond surface in dilute saline solution is shown with a frame-rate of 167 Hz. A 3-point running average filter has been applied the data to aid with visualization, however no filtering was applied to data presented in the main text.

Supplementary References

1. Rocha, P. R. F. *et al.* Electrochemical noise and impedance of Au electrode/electrolyte interfaces enabling extracellular detection of glioma cell populations. *Scientific Reports* **6**, (2016).
2. Viswam, V., Obien, M. E. J., Franke, F., Frey, U. & Hierlemann, A. Optimal Electrode Size for Multi-Scale Extracellular-Potential Recording From Neuronal Assemblies. *Frontiers in Neuroscience* **13**, (2019).
3. Abbott, J. *et al.* A nanoelectrode array for obtaining intracellular recordings from thousands of connected neurons. *Nature Biomedical Engineering* **4**, (2020).
4. Jung, D. *et al.* A 21952-Pixel Multi-Modal CMOS Cellular Sensor Array with 1568-Pixel Parallel Recording and 4-Point Impedance Sensing. in *2019 Symposium on VLSI Circuits* (IEEE, 2019). doi:10.23919/VLSIC.2019.8778043.
5. Lopez, C. M. *et al.* A 16384-electrode 1024-channel multimodal CMOS MEA for high-throughput intracellular action potential measurements and impedance spectroscopy in drug-screening applications. in *2018 IEEE International Solid - State Circuits Conference - (ISSCC)* (IEEE, 2018). doi:10.1109/ISSCC.2018.8310385.
6. Angotzi, G. N. *et al.* A high temporal resolution multiscale recording system for in vivo neural studies. in *2017 IEEE International Symposium on Circuits and Systems (ISCAS)* (IEEE, 2017). doi:10.1109/ISCAS.2017.8050617.
7. Liu, R. *et al.* High Density Individually Addressable Nanowire Arrays Record Intracellular Activity from Primary Rodent and Human Stem Cell Derived Neurons. *Nano Letters* **17**, (2017).
8. Müller, J. *et al.* High-resolution CMOS MEA platform to study neurons at subcellular, cellular, and network levels. *Lab on a Chip* **15**, (2015).
9. Ristein, J., Zhang, W. & Ley, L. Hydrogen-terminated diamond electrodes. I. Charges, potentials, and energies. *Physical Review E* **78**, (2008).
10. Momenzadeh, S. A. *et al.* Nanoengineered Diamond Waveguide as a Robust Bright Platform for Nanomagnetometry Using Shallow Nitrogen Vacancy Centers. *Nano Letters* **15**, (2015).
11. Hacquebard, L. & Childress, L. Charge-state dynamics during excitation and depletion of the nitrogen-vacancy center in diamond. *Physical Review A* **97**, (2018).
12. Bazant, M. Z., Thornton, K. & Ajdari, A. Diffuse-charge dynamics in electrochemical systems. *Physical Review E* **70**, (2004).
13. Lenzi, E. K., de Paula, J. L., Silva, F. R. G. B. & Evangelista, L. R. A Connection Between Anomalous Poisson–Nernst–Planck Model and Equivalent Circuits with Constant Phase Elements. *The Journal of Physical Chemistry C* **117**, (2013).
14. Geddes, L. A. Historical evolution of circuit models for the electrode-electrolyte interface. *Annals of Biomedical Engineering* **25**, (1997).
15. Spira, M. E. & Hai, A. Multi-electrode array technologies for neuroscience and cardiology. *Nature Nanotechnology* **8**, (2013).

16. Pippione, G., Olivero, P., Fischer, M., Schreck, M. & Pasquarelli, A. Characterization of CVD Heavily B-Doped Diamond Thin Films for Multi Electrode Array Biosensors. *physica status solidi (a)* **214**, 1700223 (2017).
17. Wang, A., Jung, D., Park, J., Junek, G. & Wang, H. Electrode–Electrolyte Interface Impedance Characterization of Ultra-Miniaturized Microelectrode Arrays Over Materials and Geometries for Sub-Cellular and Cellular Sensing and Stimulation. *IEEE Transactions on NanoBioscience* **18**, 248–252 (2019).
18. Rezek, B. *et al.* Fermi level on hydrogen terminated diamond surfaces. *Applied Physics Letters* **82**, 2266–2268 (2003).
19. Grotz, B. *et al.* Charge state manipulation of qubits in diamond. *Nature Communications* **3**, (2012).
20. Luryi, S. Quantum capacitance devices. *Applied Physics Letters* **52**, (1988).
21. Dankerl, M. *et al.* Hydrophobic Interaction and Charge Accumulation at the Diamond-Electrolyte Interface. *Physical Review Letters* **106**, 196103 (2011).
22. CHOU, H. A., FRENKEL, D. & OVADIA, M. Determination of Standard Electrode Potential E₀ for Chronic Platinum and Gold Electrodes in Rat Muscle: Implications for Biosensors and the “Anode” of Bipolar Pacing. *Pacing and Clinical Electrophysiology* **25**, 1053–1060 (2002).
23. Knöpfel, T. & Song, C. Optical voltage imaging in neurons: moving from technology development to practical tool. *Nature Reviews Neuroscience* **20**, (2019).
24. Karlsson, M. & Nikolajeff, F. Diamond micro-optics: microlenses and antireflection structured surfaces for the infrared spectral region. *Optics Express* **11**, (2003).
25. Zhang, Y. *et al.* Demonstration of diamond microlens structures by a three-dimensional (3D) dual-mask method. *Optics Express* **25**, (2017).
26. Liu, Z. *et al.* Fabrication of micro lens array on diamond surface. *AIP Advances* **9**, (2019).
27. Kehayias, P. *et al.* Solution nuclear magnetic resonance spectroscopy on a nanostructured diamond chip. *Nature Communications* **8**, (2017).
28. Capelli, M. *et al.* Increased nitrogen-vacancy centre creation yield in diamond through electron beam irradiation at high temperature. *Carbon* **143**, (2019).
29. Mindarava, Y. *et al.* Efficient conversion of nitrogen to nitrogen-vacancy centers in diamond particles with high-temperature electron irradiation. *Carbon* **170**, (2020).
30. Lühmann, T., John, R., Wunderlich, R., Meijer, J. & Pezzagna, S. Coulomb-driven single defect engineering for scalable qubits and spin sensors in diamond. *Nature Communications* **10**, (2019).
31. Garrett, D. J., Tong, W., Simpson, D. A. & Meffin, H. Diamond for neural interfacing: A review. *Carbon* **102**, 437–454 (2016).
32. Ariano, P. *et al.* Cellular adhesion and neuronal excitability on functionalised diamond surfaces. *Diamond and Related Materials* **14**, 669–674 (2005).
33. May, P. W. *et al.* Spatially controlling neuronal adhesion on CVD diamond. *Diamond and Related Materials* **23**, 100–104 (2012).
34. Dankerl, M. *et al.* Diamond Transistor Array for Extracellular Recording From Electrogenic Cells. *Advanced Functional Materials* **19**, 2915–2923 (2009).
35. Hanlon, L. *et al.* Diamond nanopillar arrays for quantum microscopy of neuronal signals. *Neurophotonics* **7**, (2020).
36. Petrakova, V. *et al.* Imaging of transfection and intracellular release of intact, non-labeled DNA using fluorescent nanodiamonds. *Nanoscale* **8**, 12002–12012 (2016).
37. Jungblut, M., Knoll, W., Thielemann, C. & Pottek, M. Triangular neuronal networks on microelectrode arrays: an approach to improve the properties of low-density networks for extracellular recording. *Biomedical Microdevices* **11**, 1269–1278 (2009).

38. Chang, J. C., Brewer, , Gregory J. & Wheeler, B. C. Microelectrode Array Recordings of Patterned Hippocampal Neurons for Four Weeks. *Biomedical Microdevices* **2**, 245–253 (2000).